ORNL/TM-2017/379

Radiation Tolerance of Controlled Fusion Welds in High Temperature Oxidation Resistant FeCrAl Alloys

Maxim N. Gussev
Kevin G. Field

August 4th, 2017

OAK RIDGE NATIONAL LABORATORY
MANAGED BY UT-BATTELLE FOR THE US DEPARTMENT OF ENERGY

ORNL/TM-2017/379

Nuclear Energy Enabling Technologies (NEET): Reactor Materials

Radiation Tolerance of Controlled Fusion Welds in High Temperature Oxidation Resistant FeCrAl Alloys

Maxim N. Gussev and Kevin G. Field

Date Published: August 5th, 2017

Prepared by
OAK RIDGE NATIONAL LABORATORY
Oak Ridge, Tennessee 37831-6283
managed by
UT-BATTELLE, LLC
for the
US DEPARTMENT OF ENERGY
under contract DE-AC05-00OR22725

CONTENTS

Page

LIST OF FIGURES

Figure **Page**

LIST OF TABLES

Table **Page**

ACKNOWLEDGMENTS

This research was sponsored by the U.S. Department of Energy, Office of Nuclear Energy, for the Nuclear Energy Enabling Technologies (NEET) program for the Reactor Materials effort. This report was authored by UT-Battelle, LLC under Contract No. DE-AC05-00OR22725 with the U.S. Department of Energy.

EXECUTIVE SUMMARY

High temperature oxidation resistant iron-chromium-aluminum (FeCrAl) alloys are candidate alloys for nuclear applications due to their exceptional performance during off-normal conditions such as a loss-of-coolant accident (LOCA) compared to currently deployed zirconium-based claddings [1]. A series of studies have been completed to determine the weldability of the FeCrAl alloy class and investigate the weldment performance in the as-received (non-irradiated) state [2,3]. These initial studies have shown the general effects of composition and microstructure on the weldability of FeCrAl alloys. Given this, limited details on the radiation tolerance of FeCrAl alloys and their weldments exist. The lack of any database on the radiation tolerance and weldability has led to the development of a welding and irradiation program to rapidly determine the irradiation performance of FeCrAl weldments.

Here, the highest priority candidate FeCrAl alloys and their weldments have been investigated after irradiation to enable a better understanding of FeCrAl alloy weldment performance within a high-intensity neutron field. The alloys examined include C35M (Fe-13%Cr-5% Al) and variants with aluminum (+2%) or titanium carbide (+1%) additions. Two different sub-sized tensile geometries, SS-J type and SS-2E (or SS-mini), were neutron irradiated in the High Flux Isotope Reactor to 1.8-1.9 displacements per atom (dpa) in the temperature range of 195°C to 559°C. Post irradiation examination of the candidate alloys was completed and included uniaxial tensile tests coupled with digital image correlation (DIC), scanning electron microscopy-electron back scattered diffraction analysis (SEM-EBSD), and SEM-based fractography. In addition to weldment testing, non-welded parent material was examined as a direct comparison between welded and non-welded specimen performance.

Both welded and non-welded specimens showed a high degree of radiation-induced hardening near irradiation temperatures of 200°C, moderate radiation-induced hardening near temperatures of 360°C, and almost no radiation-induced hardening at elevated temperatures near 550°C. Additionally, low-temperature irradiations showed the non-welded specimens to exhibit strain-induced softening (decrease in the true stress level) with increasing plastic strain during tensile testing. Fracture for the weldments was found to occur exclusively within the fusion zone. The mechanical performance of the weldment was speculated to be directly linked to variances in the radiation-induced microstructure including the formation of dislocation loops and precipitation of the Cr-rich α' phase. The localized microstructural variation within the weldments, including grain size, was determined to play a significant role in the radiation-induced microstructure. The results summarized within highlight the need for additional data on the radiation tolerance of weldments as the mechanical performance of the fusion zone was shown to be the limiting factor in the overall performance of the weldments.

1. INTRODUCTION

Several different material systems and alloy classes are currently under consideration as Accident Tolerant Fuel (ATF) forms including SiC cladding and FeCrAl alloy cladding. One of the primary performance metrics indicated for ATF applications is the material system to withstand off-normal conditions, such as a loss-of-coolant accident, which is directly related to the high-temperature oxidation resistance of the material system. SiC and FeCrAl cladding both exhibit excellent elevated temperature (>1000°C) oxidation resistance in air and steam environments. FeCrAl alloys are being heavily considered as a near term ATF concept while it is anticipated that the development of SiC cladding could be significantly lengthier [4,5]. To see the commercial maturation of the FeCrAl alloy class for ATF applications, a wide range of different performance parameters metrics need to be evaluated and well understood. One such metric is the weldability and the radiation tolerance of typical welds for the FeCrAl alloys. Welding is employed in the commercial cladding to hermetically seal the fuel pins, and hence any issues with weldability or the degradation of the weldments under normal or off-normal operation could lead to significantly higher fuel failure rates.

Preliminary studies on the weldability of the FeCrAl alloy class using several common techniques including Gas Tungsten Arc Welding (GTAW), laser beam welding (LBW), and pressure resistance welding (PRW) have been completed [6–12]. Given this, limited information on the radiation tolerance of weldments at conditions typical to commercial light water reactors (LWRs) exists. Radiation tolerance of non-weldments has seen considerably more studies and fundamental aspects on the radiation tolerance of non-welded material has been established [13–19]. It is anticipated that trends established on the non-welded material may not hold true for irradiated weldments. Localized melting within the fusion zone of the weldment leads to the disappearance of the controlled, tailored microstructure. Regions outside the fusion zone can also see localized heating. In both instances, the microstructure and the microchemistry can be significantly altered within these regions, both of which can affect the radiation tolerance of a given material system.

An active research program has been targeted at evaluating the radiation tolerance of weldments produced using LBW in candidate FeCrAl alloys. Previous activities within the program have established an alloying scheme to mitigate weld-induced cracking and to determine the baseline properties of the weldments [9]. The result is seven different candidate alloys are being investigated. One of the alloys is the reference material (C35M), two are modifications of Al from C35M (C36M and C37M), one has Nb additions to promote Laves phase formation (C35MN), and the last three have TiC dispersions at varying weight fractions (C35M01TC, C35M03TC, and C35M10TC). Alloys were designed to address specific issues including hydrogen assisted weld-induced cracking and mitigation of the embrittling Cr-rich α' phase. Welding trials on the varying alloys generally showed that welding led to a decrease in the overall strength [9]. The loss of strength was directly related to discrete changes in microstructure. Given this, welding did lead to several weldments showing sudden fracture events stemming from the possibility of porosity or inclusions within the weldments. Based on these activities, it was established that the modifications of FeCrAl alloys, both compositionally and microstructurally, can alter the weldability of the FeCrAl alloy class. Based on the completed assessments, a prioritization of further examination on the radiation tolerance of the different alloys was established with the following priority (highest listed first): C35M, C35M10TC, C37M, C35M03TC, C35M01TC, C36M, and C35MN [20].

Based on the established prioritization, a series of different studies and evaluations have been completed on the top three alloys of interest after irradiation. The alloys of interest were irradiated within the High Flux Isotope Reactor in both the SS-2E (or SS-mini) and the SS-J type configuration [21]. The following report details the characterization of top priority alloys (C35M, C35M10TC, and C37M) using advanced mechanical testing techniques within the Irradiated Materials Examination and Testing (IMET) shielded

hot cell facility and the Low Activation Materials Development and Analysis (LAMDA) facility, both of which are house at Oak Ridge National Laboratory (ORNL).

2. MATERIALS AND METHODS

2.1 Candidate FeCrAl Alloys

FeCrAl alloys C35M, C37M, and C35M10TC were selected for on-going analysis based on a prioritization schedule developed from non-irradiated weldment performance [20]. The development of these alloys and their as-received microstructure in both the parent material and the weldment have been reported in detail previously [9]. Only a brief overview regarding the details are presented here.

Production of bulk material was completed using either vacuum induction melting or arc melting followed by casting, homogenization at 1200°C in an argon gas atmosphere for 4 hours, followed by air cooling, and hot forging at 800°C with a 50% reduction in thickness (from ~25 to ~12.5 mm) to make plate-shaped samples. After that, the plates were hot rolled at 800°C with an additional ~40% reduction in thickness, and then annealed at 800°C in laboratory air for 1 hour. The final step consisted of warm-rolling at 300°C with 90% thickness reduction and annealing at 650°C for 1 hour in the air [13]. Table 1 provides the composition of the three alloys following casting.

Table 1: Candidate FeCrAl alloys processing routes and composition in weight percent.

Alloy	Fe	Cr	Al	Y	Mo	Si	Nb	C	S	O	N	P	Ti
C35M[1]	79.43	13.06	5.31	0.053	2	0.13	<0.01	0.001	<0.0003	0.0012	0.0003	0.007	<0.01
C37M[1]	77.49	13.01	7.22	0.081	1.99	0.19	<0.01	0.001	<0.0003	0.0026	0.0002	0.004	<0.01
C35M10TC[2]	78.82	12.95	5.14	0.01	1.96	0.2	<0.01	0.18	<0.0003	0.0012	0.0007	<0.002	0.71

All other elements (Zr, B, Hf, V, W, Ce, Co, Cu, La, Mn, Ni) measured to be at or below <0.01
[1]VIM ingot, [2]Arc-melt and drop cast ingot

C35M was selected as the reference alloy while C37M and C35M10TC were selected to determine the influence of composition and particle dispersions on the weldability and radiation tolerance, respectively. C35M and C37M have been predicted to straddle the boundary for GTA weldability [6] as well as the phase boundary for the Cr-rich α' phase at moderate to low temperatures (≤475°C) [22–24]. The formation of the Cr-rich α' phase is detrimental since its presence has been linked to significant hardening and embrittlement of the alloy after aging or after high-flux neutron irradiation [13,15,16]. C35M10TC contains a dispersion of TiC particles within the matrix and is predicted to act as efficient hydrogen trapping sites during welding [7] and as recombination centers for radiation-induced defects. It was also fortuitous that TiC also acts as pinning sites for grain boundaries during recrystallization and welding. Given this, it is unclear on the role of TiC dispersion on the radiation tolerance of FeCrAl alloys. Note, yttrium and molybdenum are contained within all alloys to promote high temperature oxidation resistance and strengthening at elevated temperatures, respectively. Further details regarding design and baseline properties can be found in Ref. [9].

2.2 Welding of Candidate FeCrAl Alloys

The same weldments used for non-irradiated studies [9] were used within this study. Hence, the details between all works are identical and only a brief description is provided here. Full penetration, autogenous, bead-on-plate welding produced using a pulsed laser-welding machine with operating parameters of 7 ms pulse length, 7 pulses/s, and a 2.12 mm/s welding speed was completed. Lamp energy was maintained near 100 Watts for the duration of the welding. An argon cover gas was used during welding to reduce oxidation and contamination of the weldments. Electric discharge machining was used to extract SS-J

type and SS-2E tensile specimens, Figure 1, from the weldments with the fusion zone centered in the gauge section in the cross-weld orientation. Surfaces were mechanically ground to meet dimensional requirements of the irradiation capsule. Optical inspections showed no superficial cracks or other weld-induced defects [9].

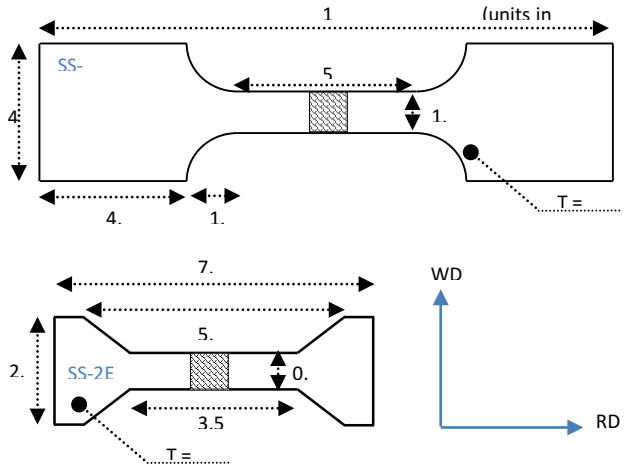

Figure 1: Tensile specimen geometries (SS-2E and SS-J2) used in the present work [21]. Pattern centered in gauge indicates the appearance of the weldment within the gauge. RD and WD show rolling (tensile) and welding (transverse) directions, respectively.

Additionally, characterization was completed using scanning electron microscopy (SEM) coupled with electron backscattered diffraction to determine general microstructural features such as grain size, texture, and grain morphology. Standard metallographic preparation resulted in "mirror-polished" specimens idealized for SEM-EBSD characterization. a JEOL JSM 6500F SEM with a field emission gun equipped with an EDAX EBSD system was used for SEM-EBSD characterization. The accelerating voltage for the investigations was 20 kV, and the working distance was 12–17 mm. The step size of the EBSD maps varied between 0.5 and 3.0 µm depending on the resolution needed for microstructural assessment. Varying step sizes were required depending on the scan locations within the weldments, e.g. 0.5 µm were used in the fine-grained parent material while 3.0 µm was used in the large grained fusion area. Step sizes were selected to maximize scan efficiency without loss of details on grain morphologies. The camera operated in a 2 × 2 binning mode at around 90–100 frames per second. Post-processing was applied using typical routines.

2.3 Irradiation within the HFIR

To date, only the low dose irradiation capsules (FCAT01, FCAT02, and FCAT03) are available for post irradiation examination. The low dose capsules contained a mix of SS-J type and SS-2E type tensile specimens of the three alloys of interest. The SS-J type tensile specimens are a common geometry, but due to their relatively large volume samples, they typically must be tested within a shielded hot cell facility. The lower volume SS-2E tensile specimens when irradiated to low-dose conditions can be moved to low activation radiological facilities resulting in the ability for more advanced mechanical performance characterization. The three low dose capsules were irradiated in the central flux trap of the High Flux Isotope Reactor (HFIR) at ORNL and designed to be irradiated at nominal temperatures of 200°C, 330°C, and 550°C. The wide temperature span provides the ability to determine generalized temperature trends at LWR and advanced reactor conditions.

Irradiation temperatures were verified using dilatometric analysis of passive silicon carbide (SiC) thermometry samples co-irradiated with the tensile specimens. The dilatometric analysis was conducted up to a maximum temperature of 600°C at a constant ramp rate of 1°C/min and a cooling rate of 2.5°C/min using a Netzsch 402 CD dilatometer and methodology described in Ref. [25]. For simplicity in describing the nominal irradiation temperature of each capsule, the capsule mean irradiation temperature (CMIT) terminology is adopted. This value represents the mean of all thermometry tested within each capsule, i.e. radial and thermal gradients within each capsule are not reflected in this value. The full irradiation details including final irradiation dose, neutron flux, and neutron fluence for each capsule are provided in Table 2.

Table 2: Summary of FeCrAl capsule irradiation conditions.

Capsule ID	Temp. ID*	CMIT (°C)	Dose (dpa)	Dose Rate (dpa/s)	Neutron Flux (n/cm^2s) E > 0.1 MeV	Neutron Fluence (n/cm^2) E > 0.1 MeV
FCAT-01	LT	194.5±37.9	1.9	9.8×10^{-7}	1.10×10^{15}	2.17×10^{21}
FCAT-02	MT	363.6±23.1	1.8	9.3×10^{-7}	1.04×10^{15}	2.05×10^{21}
FCAT-03	HT	559.4±28.1	1.9	9.8×10^{-7}	1.10×10^{15}	2.17×10^{21}

*LT: Low Temperature, MT: Middle Temperature, HT: High Temperature

2.4 Mechanical testing of sub-sized specimens

Tensile testing of the irradiated and non-irradiated SS-J type specimens were completed using a remotely controlled Instron universal testing machine. As discussed, shielding was needed due to the high sample radioactivity (>100 mrem/hr at 30 cm) of the SS-J type specimens. Testing was completed using shoulder loading at a nominal strain rate of 10^{-3} s^{-1}. Engineering strains were determined based on pre-irradiation dimensional inspection data and digitally recorded crosshead displacements. Due to the limited number of specimens available at the time of this study, only 1 specimen per configuration, welded and non-welded, and irradiation condition were completed for the SS-J type specimens. A JEOL JSM-6010A scanning electron microscopy (SEM), located in the shielded hot cell facility and remotely operated, was used to investigate the fracture surfaces of the SS-J type tensile specimens. Fractography was completed using a 5 kV beam and a 10 mm working distance.

SS-2E specimens in the irradiated and non-irradiated state were tested on a MTS Insight 2-52 one-column tensile screw machine outfitted with a 2 kN load cell. Tensile tests were completed within ORNL's LAMDA facility. Specialized grips were used to perform shoulder loading during the tests with the tests performed at room temperature using a nominal strain rate of 10^{-3} s^{-1}. Tests include determination of localized strain and stress within the SS-2E specimens using common digital image correlation (DIC) approaches. Random speckle patterns were applied using air brush techniques. Patterns were imaged using a high-resolution Allied Vision GX3300 camera equipped with a telecentric lens. Pixel resolution was determined to be nominally 5 μm. Post-test DIC analysis was determined using VIC-2D commercial software and custom software applications.

3. EXPERIMENTAL RESULTS

3.1 Microstructure prior to irradiation

The local microstructures including SEM-EBSD results have been presented for the given alloys previously [9]. The results are reproduced here for completeness. The non-irradiated, non-welded alloys showed a microstructure consistent with warm-rolled material conditions as presented in Figure 2. The alloys all exhibited some fraction of deformed (non-recrystallized) and recrystallized grains with texturing centered on the [101] corner of the unit triangle. The inverse pole figure maps shown in Figure 2 are plotted in respect to the warm-rolling direction, which is also the tensile direction, Figure 1. The majority of texturing arose from the deformed grains; recrystallized grains tended to show close-to-random texturing. For example, see alloy C37M in Figure 2.

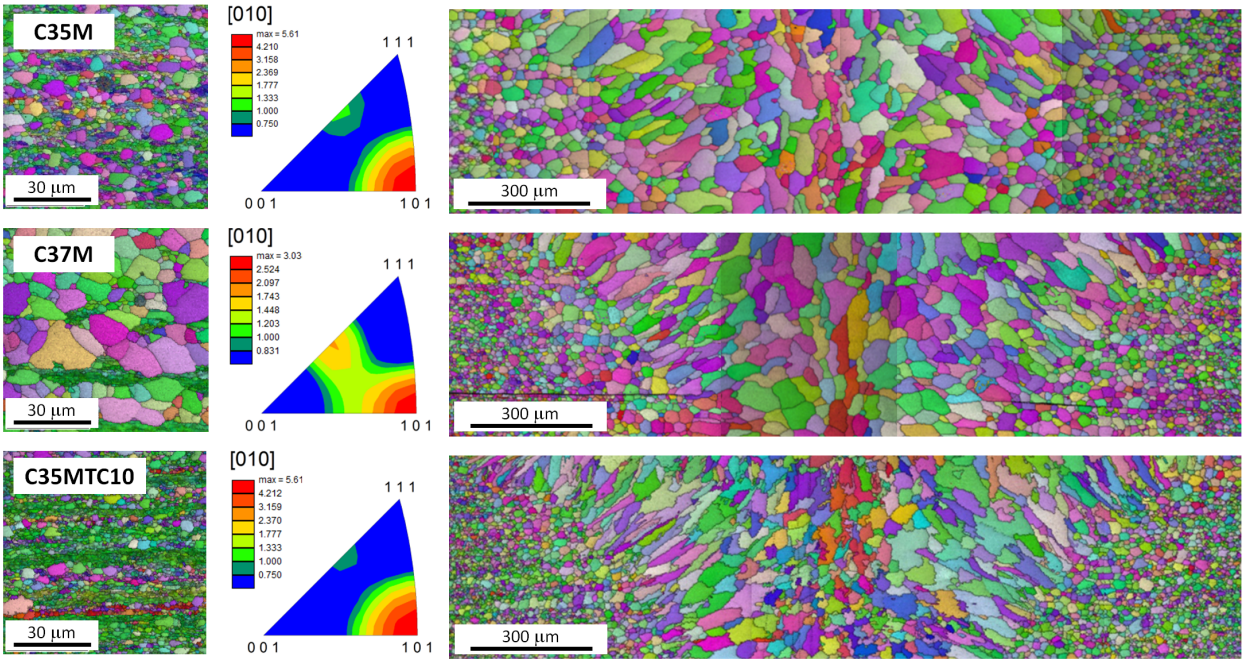

Figure 2: The structure and texture of the as-received (AR) alloys (left) and microstructure of the weldments (right). The Inverse Pole Figures (IPFs) are colored and the texture plot for the AR specimens are oriented in the tensile direction. Note different magnification level in the IPF maps.

The degree of recrystallization within the non-irradiated, non-welded alloys varied depending on alloy. Note, all alloys experienced identical post-casting processing routes. The C35M alloy experienced moderate recrystallization, whereas C37M demonstrated an almost fully (>90%) recrystallized structure with well-shaped grains, Figure 2. The TiC additions within C35M10TC resulted in significantly smaller recrystallized grains and recrystallization degree. These findings indicate a marked benefit of TiC dispersions on grain refinement in FeCrAl alloys within the given composition ranges. Small variations in the composition may lead to significant changes in the recrystallization kinetics [26] and final grain size of these alloys (e.g., C35M vs. C37M as shown in Figure 2).

SEM-EBSD was also performed on the non-irradiated, welded alloys, Figure 2. Due to the large area of the fusion zone and surrounding heat affected zone (HAZ) multiple scans were stitched together to provide a full field-of-view of the localized weldment microstructure. For C35M and C37M, welding led to the formation of relatively large grains of irregular shapes near the weldment centerline. This feature

was complemented by elongated or columnar grains which appeared roughly 200–300 μm away from the centerline. The width of the columnar-grain area was around 300 μm. Distinct areas of coarse, round-shaped grains were observed nearly 600 μm away from the centerline. For C35M10TC, the TiC dispersions limited significant grain grow during the re-melt and solidification process leading to grain sizes on the order of 3–5× smaller when compared to C35M or C37M. Additionally, grain boundaries showed a torturous nature indicating localized pinning of the grain boundaries via the TiC dispersions within the melt/matrix. The columnar-grain growth region also exhibited smaller grain sizes although elongation was more pronounced within the region for the grains in C35M10TC. Additional details on the morphology of the weldments can be found in Ref. [9].

3.2 Engineering stress-strain curves

Full, representative engineering stress-strain curves for the non-welded and welded specimens prior to and after irradiation are shown in Figure 3. Non-irradiated, non-welded specimens showed nearly identical behavior regardless of alloy: a smooth transition from elastic to plastic deformation, sometimes with very weak force drop near the yield point, moderate deformation hardening, and pronounced necking. Additionally, stress and ductility parameters were nearly comparable for all non-irradiated specimens. As provided previously [21], SS-2E results showed good matching to the mechanical tests performed on the SS-J type specimens.

Non-irradiated weldments showed lower strength parameters and lower ductility. The change in mechanical performance of the non-irradiated weldments compared to the parent material can be attributed to the localized grain structures within the fusion zone and the heat-affected zone(s) compared to the parent material, Figure 2. Alloy-to-alloy variations also existed among the non-irradiated welded specimens. The most pronounced variation was in the ductility parameters. For example, the C37M non-irradiated weldment showed lower ductility compared to other alloy weldments. Previous SEM-based fractography also showed very limited necking in this alloy. The variations between the alloys have previously been attributed to pre-existing defects such as nano-voids within the weldments of specific alloys [3].

Of primary interest is the performance of the non-welded and welded alloys after neutron irradiation. The lowest temperature irradiation capsule (194.5±37.9°C) showed the most significant changes in the mechanical properties of both the welded and non-welded specimens, Figure 3. Non-welded specimens demonstrated no load carry capacity after yield leading to zero uniform elongation. Some localized ductility remained within the non-welded specimens leading to necking and plastic strains on the order of several percent. Such a case was not found on the weldments irradiated in the lowest temperature capsule; no plastic ductility was observed including localized deformation resulting in nearly brittle fracture. Slightly higher irradiation temperatures (363.6±23.1°C) showed more favorable mechanical performance. Moderate hardening can be observed in all alloys in both the welded and non-welded state compared to their non-irradiated counterparts. In general, embrittlement (loss of total elongation) was observed in the welded specimens irradiated at 363.6±23.1°C except for the C35M alloy. The highest temperature irradiation (559.4±28.1°C) showed the least change in the stress-strain curves compared to the unirradiated counterparts. Both welded and non-welded specimens showed limited radiation-induced hardening and retention of ductility within the error of the tests.

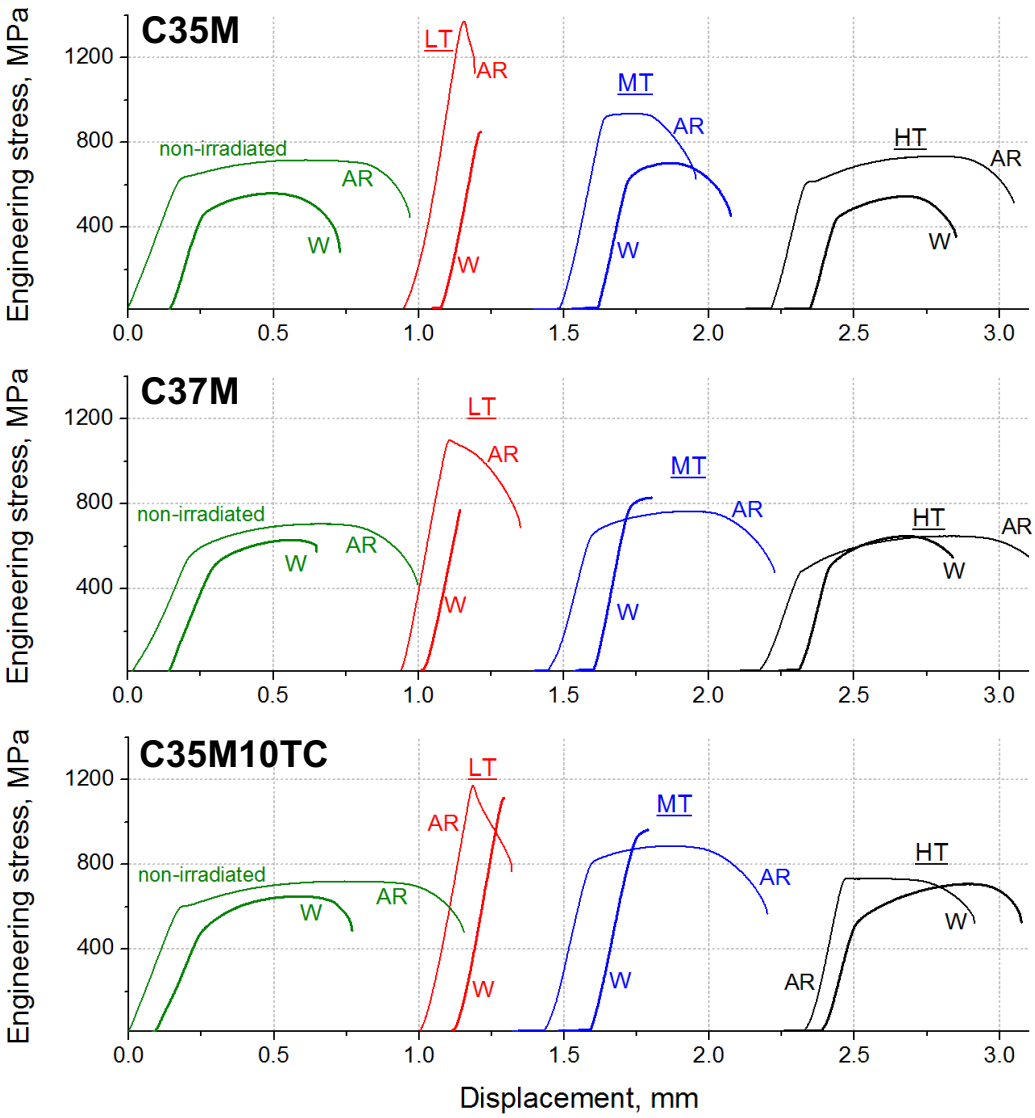

Figure 3: Representative tensile curves in the "Engineering stress vs. displacement" coordinates for non-irradiated and irradiated specimens of the investigated FeCrAl alloys (SS-Mini geometry). LT, MT, HT: low-, middle-, and high-temperature irradiation conditions –, respectively (see Table 2). AR: as-received material, W: welded specimens. Curves are offset for readability.

3.3 Fractography analysis of the tested specimens

SEM-based fractography was used in conjunction with engineering stress-strain curves to determine the fracture mechanisms in the alloys. Figure 4 shows the typical fracture surfaces for the non-welded and welded specimens after irradiation for all three conditions studied, Table 2, for C37M. Previous fractography for non-irradiated, non-welded specimens showed a ductile fracture mechanism during tensile testing [9]. The same mechanism can be seen in the alloys following both moderate (363.6±23.1°C) and elevated temperature (559.4±28.1°C) irradiation. The lowest temperature irradiation also showed dimple-like fracture surfaces indicative of ductile fracture but pronounced secondary cracks were also observed, Figure 4.

After welding, the C35M alloy demonstrated mostly ductile fracturing prior to irradiation, as discussed in [13]; no cleavage spots were observed. In contrast, after irradiation, the alloy had completely-brittle

fractures; only cleavage surfaces were observed. Welded C37M alloy revealed brittle fracture before [13] and after irradiation (Figure 4); no ductile dimples were detected.

Interestingly, the cleavage fracture mechanism, Figure 4, did not interfere with the high local ductility and neck development for the welded specimen's prior to irradiation and after high temperature irradiation, Figure 9 and Figure 5. One may speculate that fractures occurred only after reaching some stress-level threshold. In other words, below some critical stress level, the material should reveal acceptable performance. Also, an interesting aspect is the complex character of the fracture and the appearance of multiple secondary cracks in the welded specimens. In some cases, small particles and debris are visible in the SEM images (Figure 4, black arrows).

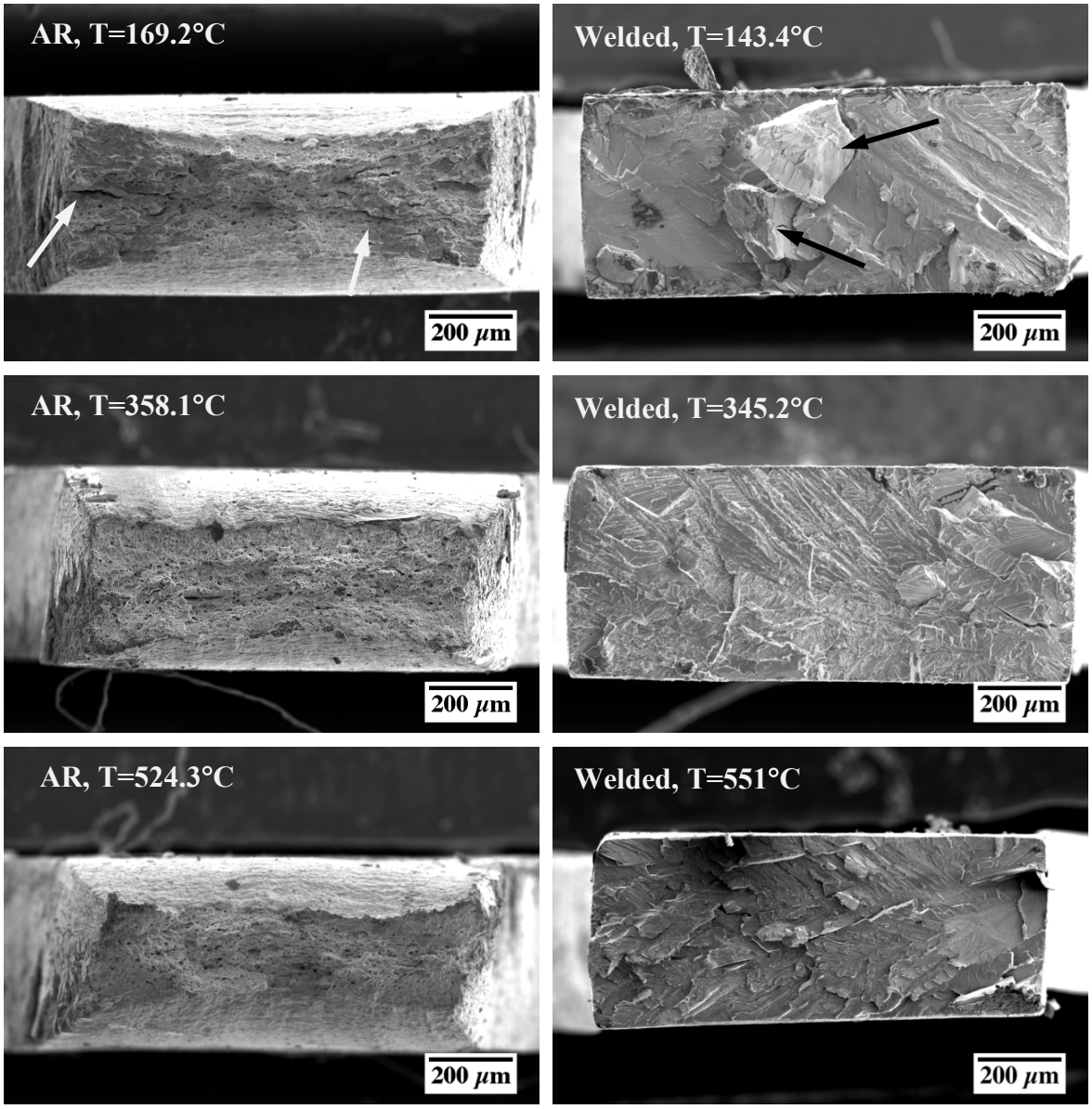

Figure 4: SEM images of the fracture surface of SS-J type specimens for C37M. AR: as-received material; irradiation temperature is given for every object. One may see brittle fracture for the welded specimens. White arrows show secondary cracks for LT-irradiated specimens. Black arrow point debris particles.

3.4 Analysis of fracture location and strain localization

Strain rate maps derived from DIC techniques on SS-2E specimens were used to determine the strain localization and location of final fracture during tensile testing. The strain maps also correlate to the strain distribution along the gauge section of the tested specimens. Figure 5 shows representative data sets from the moderate irradiation temperature condition for the C35M alloy in the welded and non-welded state. For the case of the non-welded specimen, strain was uniformly distributed across the gauge until the formal ultimate tensile strength was met and then localized necking followed. The observed results are consistent with the observed ductility from the engineering stress-strain curves. For all non-welded specimens, the location of the neck was random although typically offset from the gauge center.

Welded specimens showed different behavior before and after irradiation. Weldments showed localized strain constrained within the fusion zone and near the adjacent heat affected zone. Little to no local strain was observed in the parent material or material far from the fusion zone. Based on this analysis, it can be concluded that all weldments failed within the fusion zone indicating optimization of the welding parameters and microstructure is critical to the radiation performance of weldments.

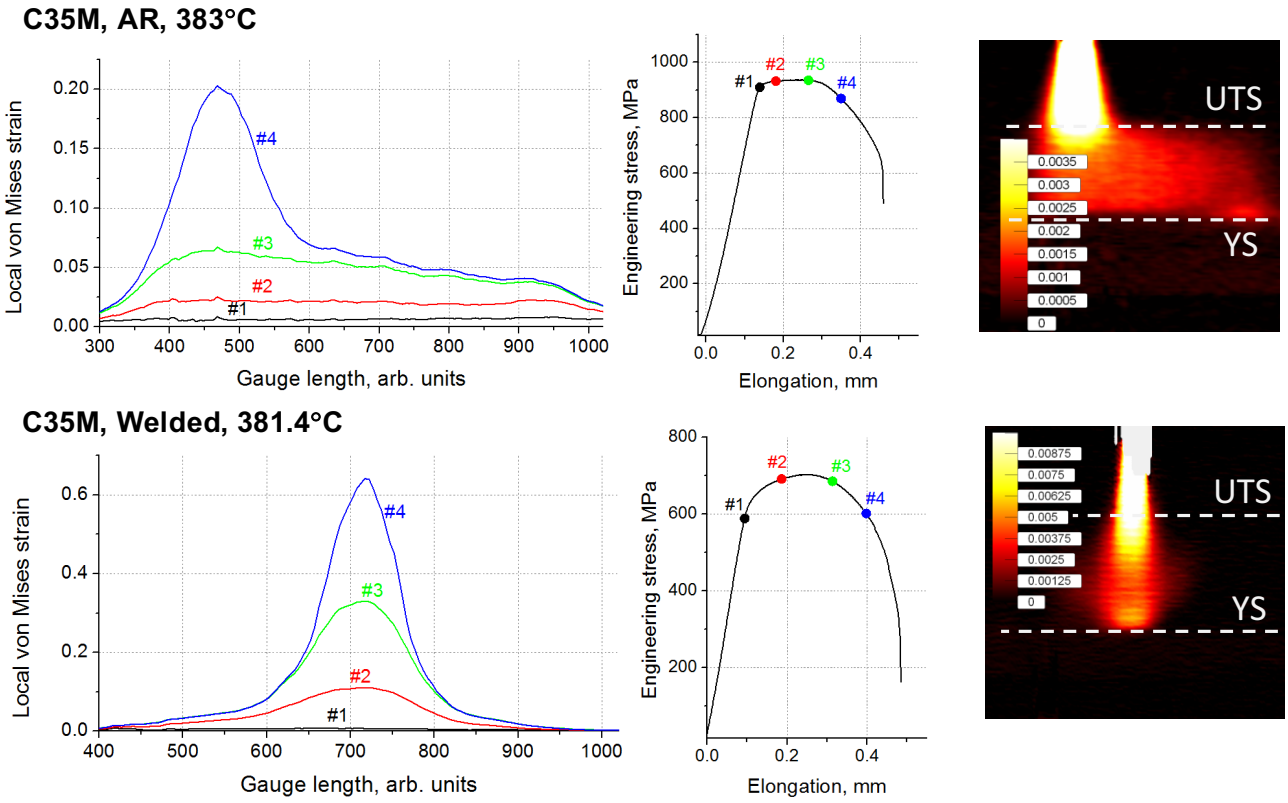

Figure 5: Left: local strain distribution (von Mises strain, Green-Lagrange strain tensor definition) along the irradiated specimen gauge (left) at different global strain levels (see the engineering tensile curves in the middle. C35M alloy specimens irradiated at MT-range. Right: strain rate maps depicting local strain rates along the gauge during the experiment.

3.5 True curves for tested specimens

DIC techniques also allow for the determination of true stress – true strain curves. Determination of true curves are essential to different modeling inputs and benchmarking efforts [27], and hence are provided here. True stress-strain curves were calculated using common approaches [28] to assess the material behavior prior to and after welding, as well as prior and after irradiation. This type of curve has no ultimate stress point or uniform elongation limit, and the true curves end at specimen fracture. During the experiment, the maximum strain value is limited by some degree because of the limitation of the experimental method used to retrieve the true curves. For instance, with the DIC approach as the main tool, the inaccuracy increases when necking begins or when a complex stress state forms [29]. Detailed analysis of the true curves usually includes some constitutive equations [30] or modern approaches based on the physics of plasticity [27], but this aspect was out of the present work scope.

Figure 6 shows the true stress-strain curves for the C35M alloy before and after irradiation. Similar curves were derived for C37M and C35M10TC. In the case of the non-irradiated specimens, welding resulted in weaker material as shown by the reduced magnitude of the curves in Figure 6. Given this, strain induced hardening remained almost unchanged between non-welded and welded specimens before irradiation. Figure 6 also indicates that irradiation at the highest temperature (559.4±28.1°C) resulted in nearly identical true stress-strain curves to those of the non-irradiated specimens – an expected result based on the strength and ductility parameters from the engineering stress-strain curves in Section 3.2.

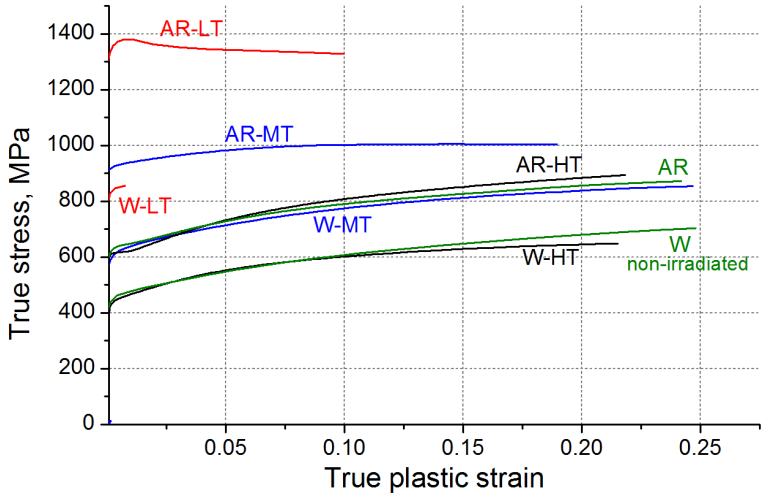

Figure 6: True stress – true strain curves for C35M alloy. Only the plastic strain is shown; elastic deformation excluded. AR and W: as-received and welded specimens, respectively. LT, MT, HT: low-, moderate-, and high-irradiation temperature.

Irradiation at 363.6±23.1°C resulted in significant irradiation hardening for both the non-welded and welded specimens. Again, the general strain-induced hardening remains nearly unchanged between the welded specimens even with an ~180 MPa shift in the higher stress area of Figure 6. For the non-welded specimens, irradiations at moderate temperature elevations led to the deformation hardening rate to decrease and become nearly 0 at ~0.10 plastic strain. This behavior is different than the non-irradiated or high temperature irradiated non-welded specimens where saturation of the deformation hardening was not observed.

The lowest temperature irradiation (194.5±37.9°C) showed significantly more radiation-induced hardening and changes to the strain-induced hardening behavior of the material. Yield stresses for the non-welded specimens are well above 1200 MPa for all alloys within this irradiation condition. Welded

specimens demonstrated strong embrittlement, and the maximum reached plastic strain value did not exceed ~1% (0.01). The most interesting case was observed for the as-received specimen: it revealed strain-induced softening (decrease in the true stress) starting at strain levels of ~0.015.

3.6 Local yield stress determination

Typically, local mechanical performance of weldments is determined using microhardness indentation arrays, for instance see Ref. [8]. This technique provides information on the mechanical performance but correlation factors such as those proposed by Busby et al. [31] are required to determine the local yield stress change of the material. Such conversion factors introduce errors into the final yield strength parameters as well as microhardness arrays have limited spatial resolution. To overcome these issues, DIC was used to also extract the local yield stress (LYS) parameters during tensile testing. The procedure used here was close to the approach offered and evaluated in Ref. [29,32]. To retrieve the LYS-curves, the approach evaluates the transition from purely an elastic behavior to an elastic-plastic behavior for each point [29,32] along the specimen gauge, using DIC images collected during the test [28]. In this manner, the spatial dependancy is based on the speckle pattern density on the specimens and the resolution of the digital capturing device.

Figure 7 shows the results of the LYS determination for all weldments for the three different alloys of interest. As shown in the data, in all cases, the minimum LYS values correspond to the weldment center with the largest grains. The LYS curves had a specific "U"-like shape and LYS values in most cases increased with the distance from the weld centerline. Weak fluctuations on the curves were caused, most likely, by local variations in the grain size. The appearance of low LYS within the gauge center, and hence the fusion zone, indicates that fracture in the specimen is occurring within the weakest portion of the specimen. Additionally, bulk strength parameters determined from the engineering stress-strain curves shown in Figure 3 are within the same range (±10%) of the lowest values for the LYS presented in Figure 7.

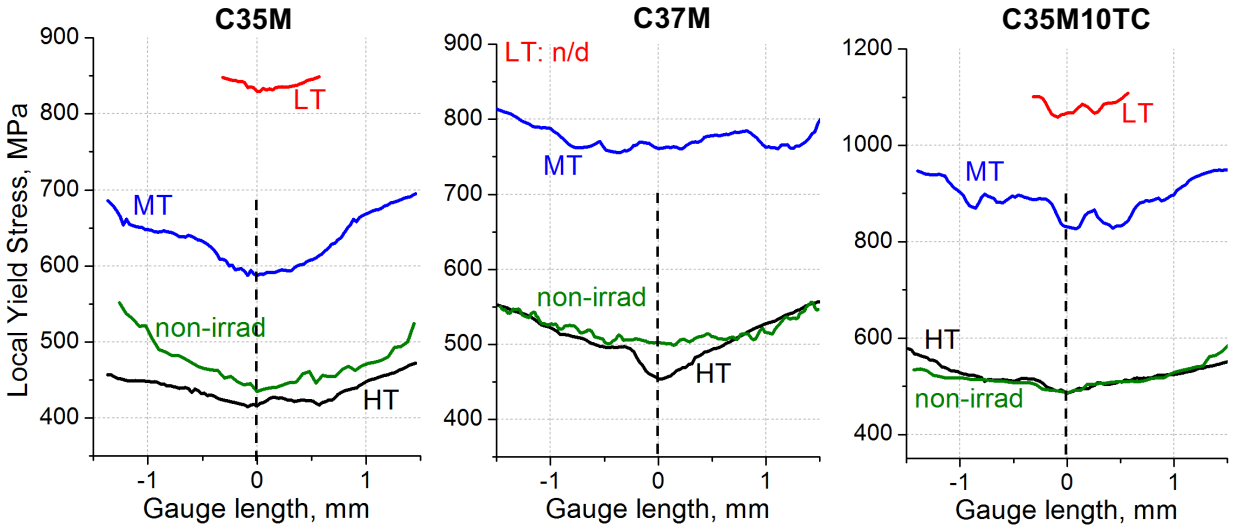

Figure 7: Local yield stress distribution along the specimen gauge center line. The zero position at the X-axis (black dashed line) corresponds to the center of the weldment, which is also gauge center. Gauge length is 3.55 mm for this specimen geometry; the portions of the LYS curves adjacent to the gauge ends were removed to avoid head influence. Note, the welded specimen of C37M alloy demonstrated brittle fracture without any signs of plastic deformation.

The lowest temperature irradiation (LT) showed only very localized deformation, as discussed prior. The result is DIC data is only present for those regions where elastic-to-plastic deformation was observed. This results in the very narrow LYS curves presented in Figure 8. Additionally, due to the short gauge length of the SS-2E geomerty (3.55 mm, Figure 1), a smooth transition from the weaker material in the weldment centerline through the HAZ to the partent material is not observed. The HAZ extends to the gauge-head transition region resulting in the gauge portion of the weldments never experiencing LYS values near that of the parent, non-welded material.

4. DISCUSSION

One major point of concern with FeCrAl alloys and their weldments is establishing the minimum and maximum use temperature within an intense neutron radiation field. Zinkle and Ghoniem [33] determined the operating windows of several material systems based on thermal creep for the upper operating window and radiation-induced hardening and embrittlement for the lower operating window. For the case of ferritic Fe-based alloy, an arbitrary fracture toughness limit was set and the window was determined to reside near 200°C. The upper window, which is dominated by thermal creep, was determined to reside near 600°C. These windows and consideration were based on typical FeCr ferritic/martensitic steels and not on the currently developing FeCrAl alloy class. Due to the large temperature range used within this study, some insight into the operating window for the FeCrAl class in comparison to the ferritic alloys in Zinkle and Ghoniem can be determined.

To better understand the temperature effects on the radiation tolerance of both the parent material and weldments, a more detailed thermal analysis of the irradiation temperature for individual specimens is adopted. The median irradiation temperature of the closest SiC thermometry specimen to each tested SS-2E and SS-J type tensile specimens was assigned for each specimen. Variation within the irradiation capsule is natural due to gradients in the neutron flux within HFIR and the radial heat flux inducing radial temperature gradients [3]. By individually assigning irradiation temperatures to each specimen, a higher fidelity in the engineering stress-strain parameters for each alloy can be developed as a function of irradiation temperature (i.e. 6 data points – 3 SS-J type and 3 SS-2E type versus only 3 data points based on CMIT).

Figure 9 shows the mechanical properties of both the welded and non-welded specimens as a function of irradiation temperature using the assigned temperature scheme. Results reflect initial indications of the hardening based on Figure 3, the lowest irradiation temperatures resulted in pronounced radiation hardening and embrittlement for all alloys. Embrittlement is indicated here by <1% total elongation. Radiation-induced hardening is seen to rapidly decrease as the irradiation temperature approaches ~400°C which is close to the ~$0.3T_m$ threshold for common FeCrAl alloys [34]. This effect is common in FeCr ferritic steels [33]. Additionally, the phase boundary for α'-precipitation reside near 500°C. A high number density of α'-precipitation has been linked to radiation induced hardening in FeCrAl alloys. The lack of significant change in the strength and ductility parameters in the specimens irradiated above >500°C is most likely directly related to the specimens residing outside of the α'-phase boundary.

Interestingly, welded specimens of C35M and C37M alloys showed smaller radiation hardening (increase in the yield stress) during low temperature irradiations, compared to the non-welded material. This effect is most likely due to varying kinetics in α'-precipitation and dislocation loop formation between the large-random orientated grains within the fusion zone versus the more fine- and textured-grains within the parent material. For example, both the grain boundaries and the dislocation networking have been shown to influence the ratio of dislocation loop types (Burgers vectors of $a/2\langle 111\rangle$ or $a\langle 100\rangle$), the local size of the dislocation loops, and the number density [14]. Additionally, Capdevila et al. investigated the precipitation kinetics of α' in an as-hot-rolled and recrystallized FeCrAl and showed faster kinetics within

the as-hot-rolled microstructure [35]. Changes in the number density and size of both dislocation loops and α' have been determined to have significant influence on the hardening behavior of FeCrAl alloys [13]. Here, it's speculated a similar effect is occurring where higher kinetics in α' precipitation are promoting greater hardening within the parent material compared to the fusion zone of the weldments but further characterization is needed to conclusively determine if this is indeed the case.

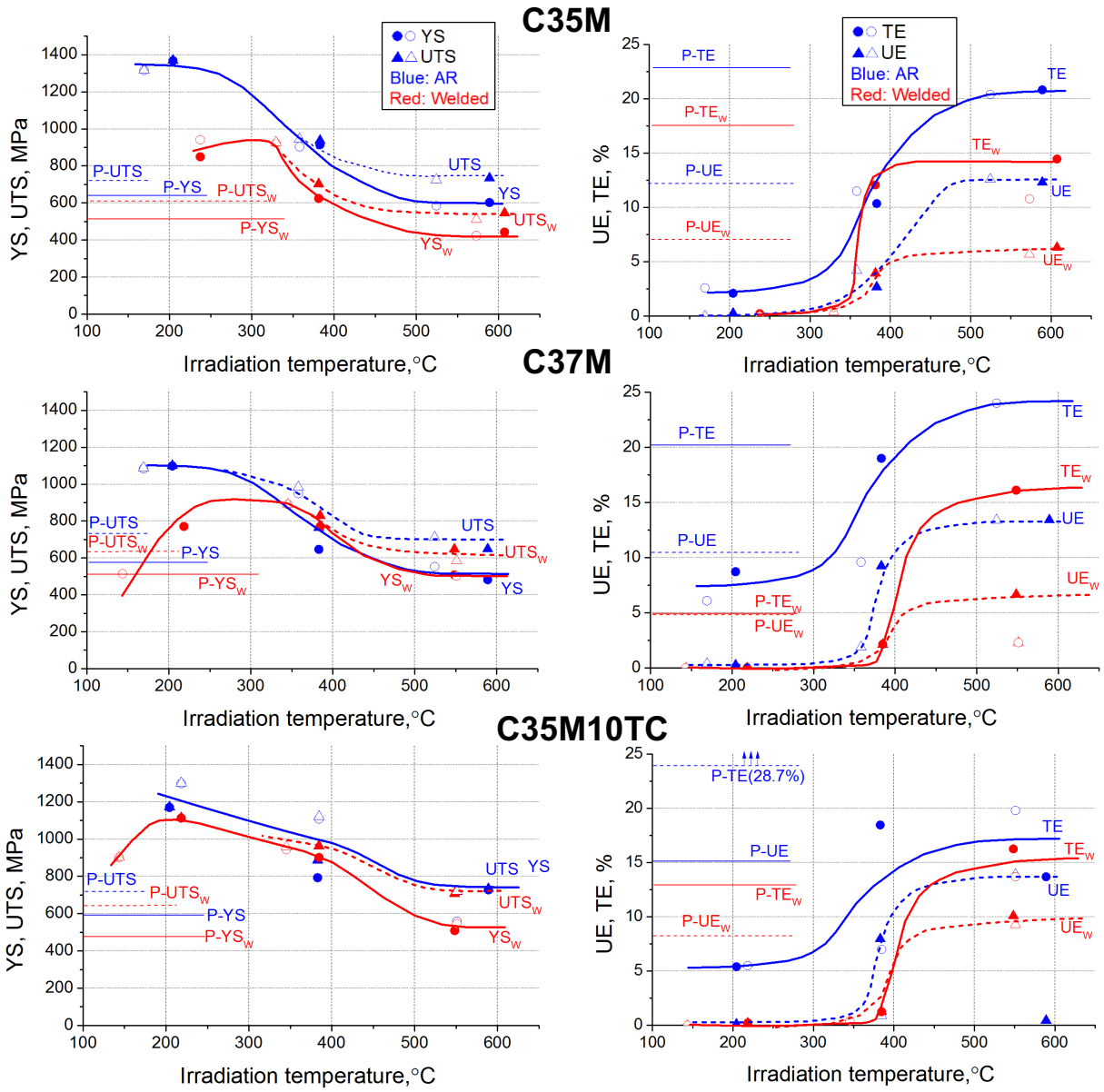

Figure 9: Mechanical properties – yield (YS) and ultimate (UTS) stress, uniform (UE) and total elongation (TE) – for the investigated alloys as a function of the individual specimen irradiation temperatures. Open and closed symbols show data points for SS-J and SS-Mini specimen geometries, respectively. Blue: as-received (AR) or parent material, red: welded specimens. Thin horizontal lines at the left and labels with P-prefix represent the baseline data for the AR and welded specimens prior to irradiation. The tests were performed at room temperature. Spline fits added to aid the eye of the reader.

The similarities in the hardening response for FeCrAl alloys compared to more traditional ferritic FeCr alloys suggest that the operating window limits for FeCrAl alloys including welded and non-welded material are within the same regime as those proposed by Zinkle and Ghoniem. An issue of concern is with respect to the fracture toughness in the low-temperature regime. Aluminum has been shown to increase the ductile to brittle transition temperature (DBTT) of FeCrAl alloys in unirradiated alloys [36]. This could be the result of the tendency for the C37M alloy to show a higher propensity for brittle fracture at temperatures below 300°C, but further work into this matter is needed. Additionally, the work here indicates no major concerns regarding radiation-induced hardening and embrittlement above 500°C, but concerns regarding thermal creep on the operating limits of the FeCrAl alloy class still remain.

5. CONCLUSIONS

The culmination of results provides insight into the ability of the different alloy designs in promoting radiation tolerance in the FeCrAl class. It appears that increased aluminum content (+2 wt.%) has little effect in reducing the radiation-induced hardening and embrittlement, especially in the temperature regimes relevant towards light water reactors. The increased propensity for embrittlement within the lowest temperature regime (<300°C) outweighs the minimal benefits observed at higher temperatures. Hence, it is suggested here that high Al modified FeCrAl alloys, at least at Cr compositions very near 13 wt.%, have no significant marked benefit for radiation tolerance or weldability of the FeCrAl alloy class. Interestingly, TiC additions (1 wt.%) did promote grain refinement in the weldments and a less pronounced transition in the hardening within the lower temperature regimes of irradiation. Given this, no marked benefits were observed in the ductility parameters after irradiation compared to the reference C35M alloys. It is concluded that the proposed benefits of alloy modifications over the reference C35M alloy are not significant enough to necessitate their use within the irradiation and welding conditions studied to date within this program. This statement may not hold true for the higher dose irradiation capsules within this program that are currently under investigation.

6. REFERENCES

[1] K.A. Terrani, S.J. Zinkle, L.L. Snead, Advanced oxidation-resistant iron-based alloys for LWR fuel cladding, J. Nucl. Mater. 448 (2013) 420–435. doi:10.1016/j.jnucmat.2013.06.041.

[2] K.G. Field, M.N. Gussev, R. Howard, First Annual Progress Report on Radiation Tolerance of Controlled Fusion Welds in High Temperature Oxidation Resistant FeCrAl Alloys, ORNL/TM-2015/770. (2015).

[3] K.G. Field, M.N. Gussev, Y. Yamamoto, R. Howard, S. Briggs, Second Annual Progress Report on Radiation Tolerance of Controlled Fusion Welds in High Temperature Oxidation Resistant FeCrAl Alloys, ORNL/TM-2016/770. (2016). http://www.ntis.gov/help/ordermethods.aspx (accessed July 16, 2017).

[4] Y. Katoh, K.A. Terrani, Systematic Technology Evaluation Program for SiC/SiC Composite-based Accident-Tolerant LWR Fuel Cladding and Core Structures: Revision 2015, ORNL/TM-2015/454. (2015). http://www.ntis.gov/help/ordermethods.aspx (accessed July 16, 2017).

[5] M. Snead, L.L. Snead, K.A. Terrani, K.G. Field, A. Worrall, K.R. Robb, et al., Technology Implementation Plan ATF FeCrAl Cladding for LWR Application, ORNL/TM-2014/353. (2015).

[6] J.R. Regina, J.N. Dupont, A.R. Marder, The effect of chromium on the weldability and microstructure of Fe-Cr-Al weld cladding, Weld. J. 86 (2007) 170–178.

[7] J.N. Dupont, J.R. Regina, K. Adams, Improving the weldability of fecral weld overlay coatings, Foss. Energy Mater. Conf. (2007) 131–137.

[8] K.G. Field, M.N. Gussev, Y. Yamamoto, L.L. Snead, Deformation behavior of laser welds in high temperature oxidation resistant Fe–Cr–Al alloys for fuel cladding applications, J. Nucl. Mater. 454 (2014) 352–358. doi:10.1016/j.jnucmat.2014.08.013.

[9] M.N. Gussev, K.G. Field, Y. Yamamoto, Design, Properties, and Weldability of Advanced Oxidation-Resistant FeCrAl Alloys, Mater. Des. 129 (2017) 227–238.

[10] J. Gan, E. Perez, D.C. Haggard, N. Jered, Summary Report on ATF Cladding Alloy Weld Development Fuel Cycle Research & Development Advanced Fuels Campaign, INL/LTD-14-31551. (2014).

[11] J. Gan, E. Perez, D.C. Haggard, N. Jerred, Status Report on Thin-Walled Cladding Weld Development and Test Fuel Cycle Research & Development Advanced Fuels Campaign, INL/LTD-16-39760. (2016).

[12] J. Gan, E. Perez, D.C. Haggard, N. Jerred, Status Report on Weld Development for FeCrAl Thin-Wall Cladding for LWR Accident Tolerant Fuels Fuel Cycle Research & Development Advanced Fuels Campaign, INL/LTD-15-36583. (2015).

[13] K.G. Field, X. Hu, K.C. Littrell, Y. Yamamoto, L.L. Snead, Radiation tolerance of neutron-irradiated model Fe-Cr-Al alloys, J. Nucl. Mater. 465 (2015) 746–755. doi:10.1016/j.jnucmat.2015.06.023.

[14] K.G. Field, S.A. Briggs, X. Hu, Y. Yamamoto, R.H. Howard, K. Sridharan, Heterogeneous dislocation loop formation near grain boundaries in a neutron-irradiated commercial FeCrAl alloy, J. Nucl. Mater. 483 (2017) 54–61. doi:10.1016/j.jnucmat.2016.10.050.

[15] S.A. Briggs, P.D. Edmondson, Y. Yamamoto, C. Littrell, R.H. Howard, C.R. Daily, et al., A combined APT and SANS investigation of alpha prime phase precipitation in neutron-irradiated model FeCrAl alloys, Acta Mater. 129 (2016) 217–228.

[16] P.D. Edmondson, S.A. Briggs, Y.Yamamoto, R.H. Howard, K. Sridharan, K.A. Terrani, et al., Irradiation-enhanced α′ precipitation in model FeCrAl alloys, Scr. Mater. 116 (2016) 112–116. doi:10.1016/j.scriptamat.2016.02.002.

[17] J. Haley, S.A. Briggs, P.D. Edmondson, K. Sridharan, S. Lozano-perez, K.G. Field, et al., Dislocation Loop Evolution During In-situ Ion Irradiation of Model FeCrAl Alloys, Submitt. to Acta Mater. (2017) 1–37.

[18] N. Raghavan, R. Dehoff, S. Pannala, S. Simunovic, M. Kirka, J. Turner, et al., Numerical modeling of heat-transfer and the influence of process parameters on tailoring the grain morphology of IN718 in electron beam additive manufacturing, Acta Mater. 112 (2016) 303–314. doi:10.1016/j.actamat.2016.03.063.

[19] K.G. Field, S.A. Briggs, K. Sridharan, R.H. Howard, Y. Yamamoto, Mechanical Properties of Neutron-Irradaited Model and Commercial FeCrAl Alloys, J. Nucl. Mater. 489 (2017) 118–128.

[20] M.N. Gussev, K.G. Field, Y. Yamamoto, The Analysis of the General Performance and Mechanical Behavior of Unirradiated FeCrAl Alloys Before and After Welding, ORNL/TM-

2016/201. (2016). https://info.ornl.gov/sites/publications/Files/Pub62814.pdf (accessed July 16, 2017).

[21] M.N. Gussev, R.H. Howard, K.A. Terrani, K.G. Field, Sub-size tensile specimen design for in-reactor irradiation and post-irradiation testing, Nucl. Eng. Des. 320 (2017) 298–308. doi:10.1016/j.nucengdes.2017.06.008.

[22] S. Kobayashi, T. Takasugi, Mapping of 475°C embrittlement in ferritic Fe–Cr–Al alloys, Scr. Mater. 63 (2010) 1104–1107. doi:10.1016/j.scriptamat.2010.08.015.

[23] J. Ejenstam, M. Thuvander, P. Olsson, F. Rave, P. Szakalos, Microstructural stability of Fe-Cr-Al alloys at 450–550 °C, J. Nucl. Mater. (2014). doi:10.1016/j.jnucmat.2014.11.101.

[24] W. Li, S. Lu, Q.-M. Hu, H. Mao, B. Johansson, L. Vitos, The effect of Al on the 475°C embrittlement of Fe–Cr alloys, Comput. Mater. Sci. 74 (2013) 101–106. doi:10.1016/j.commatsci.2013.03.021.

[25] A.A. Campbell, W.D. Porter, Y. Katoh, L.L. Snead, Method for analyzing passive silicon carbide thermometry with a continuous dilatometer to determine irradiation temperature, Nucl. Instruments Methods Phys. Res. Sect. B Beam Interact. with Mater. Atoms. 370 (2016) 49–58. doi:10.1016/j.nimb.2016.01.005.

[26] S. Dziaszyk, E.J. Payton, F. Friedel, V. Marx, G. Eggeler, On the characterization of recrystallized fraction using electron backscatter diffraction: A direct comparison to local hardness in an IF steel using nanoindentation, Mater. Sci. Eng. A. 527 (2010) 7854–7864. doi:10.1016/j.msea.2010.08.063.

[27] A. Patra, D.L. McDowell, Crystal plasticity investigation of the microstructural factors influencing dislocation channeling in a model irradiated bcc material, Acta Mater. 110 (2016) 364–376. doi:10.1016/j.actamat.2016.03.041.

[28] C. Leitão, I. Galvão, R.M. Leal, D.M. Rodrigues, Determination of local constitutive properties of aluminium friction stir welds using digital image correlation, Mater. Des. 33 (2012) 69–74. doi:10.1016/j.matdes.2011.07.009.

[29] M.O. Acar, Gungor, Salih, Experimental and numerical study of strength mismatch in cross-weld tensile testing How to cite, (n.d.). doi:10.1177/0309324715593699.

[30] M.N. Gussev, T.S. Byun, J.T. Busby, Description of strain hardening behavior in neutron-irradiated fcc metals, J. Nucl. Mater. 427 (2012) 62–68. doi:10.1016/j.jnucmat.2012.04.017.

[31] J.T. Busby, M.C. Hash, G.S. Was, The relationship between hardness and yield stress in irradiated austenitic and ferritic steels, J. Nucl. Mater. 336 (2005) 267–278. doi:10.1016/j.jnucmat.2004.09.024.

[32] M. Turski, M.C. Smith, P.J. Bouchard, L. Edwards, P.J. Withers, Spatially Resolved Materials Property Data From a Uniaxial Cross-Weld Tensile Test, J. Press. Vessel Technol. 131 (2009) 61406. doi:10.1115/1.4000196.

[33] S.. Zinkle, N.. Ghoniem, Operating temperature windows for fusion reactor structural materials, Fusion Eng. Des. 51–52 (2000) 55–71. doi:10.1016/S0920-3796(00)00320-3.

[34] J.W. McMurray, R. Hu, S.V. Ushakov, D. Shin, B.A. Pint, K.A. Terrani, et al., Solid-liquid phase

equilibria of Fe-Cr-Al alloys and spinels, J. Nucl. Mater. 492 (2017) 128–133. doi:10.1016/j.jnucmat.2017.05.016.

[35] C. Capdevila, M.K. Miller, K.F. Russell, J. Chao, J.L. González-Carrasco, Phase separation in PM 2000™ Fe-base ODS alloy: Experimental study at the atomic level, Mater. Sci. Eng. A. 490 (2008) 277–288. doi:10.1016/j.msea.2008.01.029.

[36] I. Kornilov, Alloys of Iron-Chromium-Aluminum, Vol 1, Academy of Sciences, Moscow, 1945.